The mantle transition zone dynamics as revealed through seismic anisotropy

J.-P. Montagner, G. Burgos, Yann Capdeville, Éric Beucler, A. Mocquet

To cite this version:

J.-P. Montagner, G. Burgos, Yann Capdeville, Éric Beucler, A. Mocquet. The mantle transition zone dynamics as revealed through seismic anisotropy. Tectonophysics, 2021, 821, pp.229133. ⟨10.1016/j.tecto.2021.229133⟩. ⟨hal-03594722⟩

submitted to *Tectonophys.*

The mantle transition zone dynamics as revealed through seismic anisotropy.

J.-P. Montagner[1], G. Burgos[3], Y. Capdeville[2], E. Beucler[2], A. Mocquet[2]

[1] *Seismology Laboratory, Institut de Physique du Globe UMR-CNRS 7154, 1 rue Jussieu 75238 Paris Cedex 05, France*

[2] *Laboratoire de Planétologie et Géodynamique, Université de Nantes, France*

[3] *C.E.A., DAM, DIF, 91297 Arpajon Cedex, France*

SUMMARY

The mantle transition zone (MTZ) of the Earth lies between 410 and ∼1000 km in depth and has a key role in mantle convection processes. In particular, the discontinuity at 660 km and its associated endothermic mineralogical transformation can slow or inhibit the passage of matter between the upper and lower mantle. The MTZ thus acts as a boundary layer within the mantle. The depth variations of radial and azimuthal seismic anisotropies enable the detection of boundary layers within the mantle. However, the 3D imaging is difficult due to the lack of sensitivity of surface waves of fundamental modes, and the poor global coverage of this depth range by body-wave data. We present a new 3D general anisotropy model (both radial and azimuthal anisotropies) of the mantle down to 1200 km in depth using surface-wave overtone datasets. We find that there is little seismic anisotropy in most of the MTZ, except below subduction zones around the Pacific Ocean and, more surprisingly, in a large area beneath eastern Eurasia where the Pacific subducting plate is stagnant. Seismic anisotropy is usually associated with intense deformation processes but also possibly to water transportation or to fine layering. This significant anisotropy in this part of MTZ might reveal a large water 'reservoir' associated with hydrous minerals or a strong stratification. It reflects a complex history beneath central Asia, where the Tethys, Izanagi and Pacific plates appear to have strongly interacted during the last 100 My, having subducted in orthogonal directions under the Asian continent, with the Tethys plate descending into the lower mantle, and the Izanagi plate remaining stagnant in the MTZ. The Asian continent is the only region in the world where subducting slabs originating from different plates can interact. This unique slab distribution might explain why some plates descend while others remain in the lower transition zone.

Key words: Anisotropy, Surface waves, Tomography, Mantle Transition Zone

1 INTRODUCTION: TRANSITION ZONE STRUCTURE AND ANISOTROPY

The role of the mantle transition zone (MTZ) in the global dynamics of the Earth has been debated for many decades, and is related to the long-standing debate on a whole mantle versus two-layer convection. Here, we consider the MTZ in a broad sense, as located around the 660-km discontinuity, and divided into the upper transition zone (410-660 km) UMTZ and the lower transition zone (660-1000 km) LMTZ. There is no doubt thanks to seismic tomography, that plates can descend through the MTZ into the lower mantle in most subduction zones, although their final fate can be diverse (van der Hilst et al. 1997; Fukao et al. 2002). The transfer budget between material subducting into the lower mantle and material remaining in the upper mantle is poorly known, which makes the nature of the MTZ controversial. There were also seismic observations showing a change in seismic properties around 920km depth since Kawakatsu & Niu (1994). A change in the shear velocity spectrum was recently found around 1000km depth (Durand et al. 2017), which might correspond to the lower limit of LMTZ. Are the 410 km and 660 km discontinuities only due to phase changes and mineralogical transformation, or is the MTZ a chemical boundary between the upper and lower mantles that strongly limits the flow between them?

An efficient way to investigate the mantle flow circulation is to map the seismic anisotropy for this depth range (Montagner & Kennett 1996; Karato 1998). Seismic anisotropy is related to the dependence of seismic wave velocity on the direction of propagation. It can have multiple causes at microscopic and macroscopic scales. Most mantle minerals are strongly anisotropic (Mainprice 2015), and anisotropy is investigated with respect to the symmetry axes of minerals. Following the pioneering work of Nicolas et al. (1973, 1980), the fast axis of olivine, the main constituent of the uppermost mantle, tends to align in the flow direction (Christensen & Lundquist 1982), according to its lattice or crystal preferred orientation (later on referred to as LPO or CPO). This microscopic anisotropic property can remain at very large scales, provided that the deformation field is coherent at scales larger than the seismic wavelength, opening the possibility to map mantle convection through the orientation of seismic anisotropy. In the MTZ, olivine and pyroxenes transform into wadsleyite (410-520km depth range), ringwoodite (520-660km depth range) and garnet, and ultimately into Mg and Ca perovskite (Mg-perovskite now named Bridgmanite), ilmenite and ferropericlase (also named magnesiowüstite). The mechanisms of alignment producing this intrinsic anisotropy in the MTZ are still being debated (Tommasi et al. 2004; Kawazoe et al. 2013). Other processes can give rise to seismic anisotropy at these great depths (named extrinsic anisotropy), such as fluid inclusion oriented distribution (although this might be a secondary effect in the deep mantle), or fine layering of isotropic material with very different velocities, which also creates a specific case of anisotropy: radial anisotropy (Backus 1962). Radial anisotropy is characterized by five independent elastic parameters (Love 1944) and no horizontal azimuthal velocity variations. The corresponding medium is a transversely isotropic medium with a vertical symmetry axis, which is usually known as the vertical transverse isotropy (VTI) medium. An example of such a finely layered or laminated medium with partial melting is illustrated by the millefeuilles model of Kawakatsu et al. (2009) of the asthenosphere. Even though the interpretation of observed anisotropy is non-unique, for large-scale mapping of fast directions of velocities, we need both radial and azimuthal anisotropies, which provide unique information on convective flows in the mantle (Tanimoto & Anderson 1984; Montagner 2002) and which can be compared to geodynamic models (e.g. Gaboret et al. (2003); Becker et al. (2003); Simmons et al. (2009); Long & Becker (2010) ...).

Seismic data enable us to observe these two main kinds of anisotropy: radial anisotropy, as above, which only requires a VTI medium to explain the Rayleigh-Love discrepancy (Anderson 1961), and azimuthal anisotropy of different body waves since the first observations on Pn (Hess 1964) and SKS splitting (Vinnik et al. 1984; Silver & Chan 1991), and surface waves at the regional (Forsyth 1975) and global (Montagner & Tanimoto 1991) scales. A VTI model is characterized by 5 parameters A, C, F, L, N (Love 1944), but for the inversion technique, they are recombined as $V_{PH}, V_{SV}, \phi = C/A = (V_{PV}/V_{PH})^2, \xi = N/L = (V_{SH}/V_{SV})^2, \eta = F/(A-2L)$. The corresponding sensitivity kernels are modified accordingly. Among the five independent elastic parameters of a VTI medium, the most easily accessible parameters are the V_{SV} velocity and the ξ parameter, which expresses the difference in the velocities between horizontally and vertically polarized S-waves ($\xi = (\frac{V_{SH}}{V_{SV}})^2$). A correct account of the crustal structure is mandatory to avoid a bias between the shallow structure and the deep structure, especially the radial anisotropy. This non-linear effect was first made evident by Montagner & Jobert (1988) and later on carefully investigated by Marone & Romanowicz (2007); Ferreira et al. (2010); Chang et al. (2015); Chang & Ferreira (2017). We make use of the crustal model of Burgos et al. (2014) derived from the joint inversion of short period group and phase velocities (periods of 15-40s). This kind of simple ξ anisotropy was introduced for the 1D spherically symmetric preliminary reference earth model (PREM) in the uppermost 220 km of the mantle (Dziewonski & Anderson 1981). Azimuthal anisotropy cannot be explained by a VTI model and requires instead a more complex model of anisotropy. When derived from surface waves, additional eight parameters are necessary (Montagner & Nataf 1986), with the best-resolved azimuthal parameters being the modulus G and its associated angle Ψ_G related to the azimuthal variation of V_{SV}.

For several decades, there has been good observational evidence for radial and azimuthal seismic anisotropies in the top 300 km of the upper mantle and in the bottom D”-layer. In the transition zone, 1D radial anisotropy was introduced to explain eigenfrequency data (Montagner & Kennett 1996), and it was extensively investigated later (Beghein et al. 2008). Since then, several global tomographic models (Kustowski et al. (2008); Panning et al. (2010); Moulik & Ekström (2014); Auer et al. (2014); French & Romanowicz (2014); Chang et al. (2015)) have displayed the radial anisotropy parameter ξ and have shown that there might be some secondary maximum (although small) of radial anisotropy in the MTZ. Some hints of azimuthal anisotropy in the MTZ (Vinnik & Montagner 1996; Wookey et al. 2002) have been provided by different kinds of body-wave data (e.g., P-to-S receiver functions, shear-wave splitting), which have demonstrated lateral variations in anisotropy in the transition zone. On a global scale, the first long-wavelength azimuthal anisotropic 3D structure in the MTZ (Trampert & van Heijst 2002) has been obtained by the inversion of Love wave overtone data, which have a limited, although significant, radial resolution in this depth range. Its lateral resolution, more than 5000 km, was too poor to gain insights into the coupling and transfer of matter between the upper and lower mantles. More recent tomographic models displayed azimuthal anisotropy distributions down to the transition zone (Yuan & Beghein 2013; Debayle et al. 2016; Schaeffer et al. 2016), but the agreement between them is rather poor (Huang et al. 2019). The discrepancies might be due to the fact that rms amplitude of the lateral variations in MTZ was found to be very small (about 1%, within the error bars), and to be much smaller than in the uppermost and lowermost mantle (the D”-layer).

2 ANISOTROPY TOMOGRAPHY FROM OVERTONE DATA

In this study, we combine two datasets of surface wave (Rayleigh and Love waves) overtones (higher modes), (Beucler & Montagner 2006; Visser et al. 2008) using different methods and different data. The merged dataset improves the global coverage of the Earth, and enables us to derive a global 3D map of the radial and azimuthal seismic anisotropies in the MTZ down to the mid-mantle ($\sim$ 1200 km). The merged dataset improves the global coverage of the Earth. It enables us to derive a global 3D map of the radial and azimuthal seismic anisotropies in the MTZ down to the mid-mantle ($\sim$1200 km). This model has a lateral resolution of 1000 km down to a depth of 1200 km. It also includes phase velocities of the higher modes of Rayleigh waves up to order 6, and higher modes of Love waves up to order 5. In the period range of 35 s to 250 s, the number of measurements of the merged dataset varies from 70000 for the fundamental Rayleigh mode (and 50000 for the fundamental Love mode) down to 30000 for the 6^{th} Rayleigh higher mode (and 8500 for the 5^{th} Love higher mode). The measurement techniques are different for each of the datasets, but both include data uncertainties. Beucler & Montagner (2006) uses the roller-coaster algorithm (Beucler et al. 2003) that clusters close events and extracts the individual phase velocities for each overtone by non-linear inversion. Visser et al. (2008) uses a model-space search approach (Yoshizawa & Kennett 2002). Several tests have been performed to check the compatibility of each of the datasets, by doing separate inversions (regionalizations of phase velocities at different periods), and joint inversions of the datasets (Burgos 2013) . The path and the azimuthal coverages for the fundamental modes of Rayleigh and Love waves are presented in Figures 1 and 2 of Burgos et al. (2014). Path and azimuthal coverages for overtones have similar distributions but with a smaller density.

We did not find large discrepancies between the two datasets, and the data of the higher mode phase velocities were jointly regionalized by taking into account their respective error bars (Figures A1 and A2). The 3D anisotropic tomographic method is an improved version of a classical two-step inversion procedure (Montagner 1986) based on gradient least-squares optimization (Tarantola & Valette 1982). The first step consists in regionalizing the measured phase (or group) velocities at different periods along the different paths in order to get the global geographical distribution of velocities. The second step is devoted to the inversion at depth of these velocity distributions in order to retrieve the 3D-distributions of seismic velocities and anisotropic parameters. The complete technique is detailed in the Appendix. The output tomographic model consists of the V_S velocity and some robust anisotropic parameters, $\xi = (\frac{V_{SH}}{V_{SV}})^2$, the S-radial anisotropy, G, with Ψ_G expressing the horizontal azimuthal dependence of V_{SV} velocity ($V_{SV} = V_{SV_0} + G\cos(2(\Psi - \Psi_G))$), and to a lesser extent, E, with Ψ_E expressing the azimuthal dependence of V_{SH} velocity ($V_{SH} = V_{SH_0} + E\cos(4(\Psi - \Psi_E))$).

Sensitivity kernels computed in PREM show why higher modes make it possible to obtain good depth resolution down to 1200 km, well below the upper (410-660 km) and lower (660-1000 km) MTZ, which are the main focus of the present study. Figure A3 (see Appendix) shows examples of the sensitivity kernels of Rayleigh and Love waves, respectively, with respect to SV-wave and SH-wave velocities for different higher modes. The maximum sensitivity at a given period increases with the order n of the higher mode. For example, at 51 s, the 4^{th} Rayleigh higher mode (Figure A3a) has a maximum sensitivity in V_{SV} at 800 km in depth. The sensitivity of Rayleigh waves to V_{SH} is small, whereas the higher modes of Love waves can also be very sensitive to V_{SV}. This property was used by Trampert & van Heijst (2002) to retrieve SV-wave anisotropy in the MTZ by using only the Love wave data. Parameter G (and similarly, parameter E) associated with the $2-\psi$ (and $4-\psi$) azimuthal dependence of SV-waves (resp. SH-waves) has the same kernel as V_{SV} (resp. V_{SH}), and therefore it can also be recovered down to the mid-mantle at 1200 km in depth (even though only the results down to 800 km in depth are presented here). V_{SV}, V_{SH}, G and E are the most robust parameters that can be retrieved by inversion at depth of the higher mode phase velocity distributions. In the second step of the tomographic technique, the inversion at depth of all of the azimuthal dependence functions of the Rayleigh and Love wave local phase velocities is performed at every point, to retrieve these most robust elastic parameters. The local crustal structure was previously derived by Burgos et al. (2014). PREM (Dziewonski & Anderson 1981) is used below the crust as the starting reference model. But after inversion, the global average ξ_{ref} of ξ is the new reference radial anisotropy model.

The tomographic model at 100 km in depth (Figure 1 Top) shows what we expect in terms of the S-wave velocity and azimuthal anisotropy distributions. The ridges and back-arc zones are slow, the old continents are very fast. For most oceanic plates, the azimuthal anisotropy correlates well with the plate motions, and the radial anisotropy parameter ξ is close to the PREM value (we only represent $\delta\xi$, the deviation with respect to PREM). Deeper in the MTZ, the amplitude of the heterogeneities is largely decreased, but the slab signature is perfectly visible, not only in the upper transition zone UMTZ (Figure 1Middle, left, 500-km depth), but also in the lower transition zone LMTZ (Figure 1 Bottom, left, 800-km depth). The azimuthal anisotropy parameter G is small in most of the oceanic areas (with a variance of 0.3% at 500km and 0.1% at 800km, smaller than the error bars $\sim 0.5-1\%$), but relatively large ($> 1\%$) in most of the subduction zones, and surprisingly below some parts of continents, in particular below Asia. Our results differ from Yuan & Beghein (2013) who found distributed azimuthal anisotropy with a larger amplitude, but in correct agreement with Schaeffer et al. (2016); Debayle et al. (2016) who found a small rms amplitude in the UMTZ. The differences between models might be due to the joint inversion of different Rayleigh and Love wave datasets with different inversion techniques. The radial anisotropic parameter ξ in UMTZ is also much smaller than in the uppermost 300 km of the mantle, and it shows a patchy pattern. The distribution of parameter ξ (Figure 1 Right) at 500 km depth is also very patchy and slightly above the errors bars only below the subduction zones, western Africa and Central Asia. The error bars are calculated as the diagonal terms of the a posteriori covariance function of parameters (Montagner 1986). At 800 km in depth (Figure 1Bottom), the pattern of ξ is completely different since it is almost everywhere below the error bars, but displays significant negative values below western America, central Africa and central Asia.

The lateral heterogeneities can be expanded in terms of the spherical harmonics and their power spectrum is computed to determine how the amplitudes of the heterogeneities in the S-wave velocity (Figure 2 Left) and azimuthal anisotropy (Figure 2 Right) vary at depth. The angular order ℓ of power

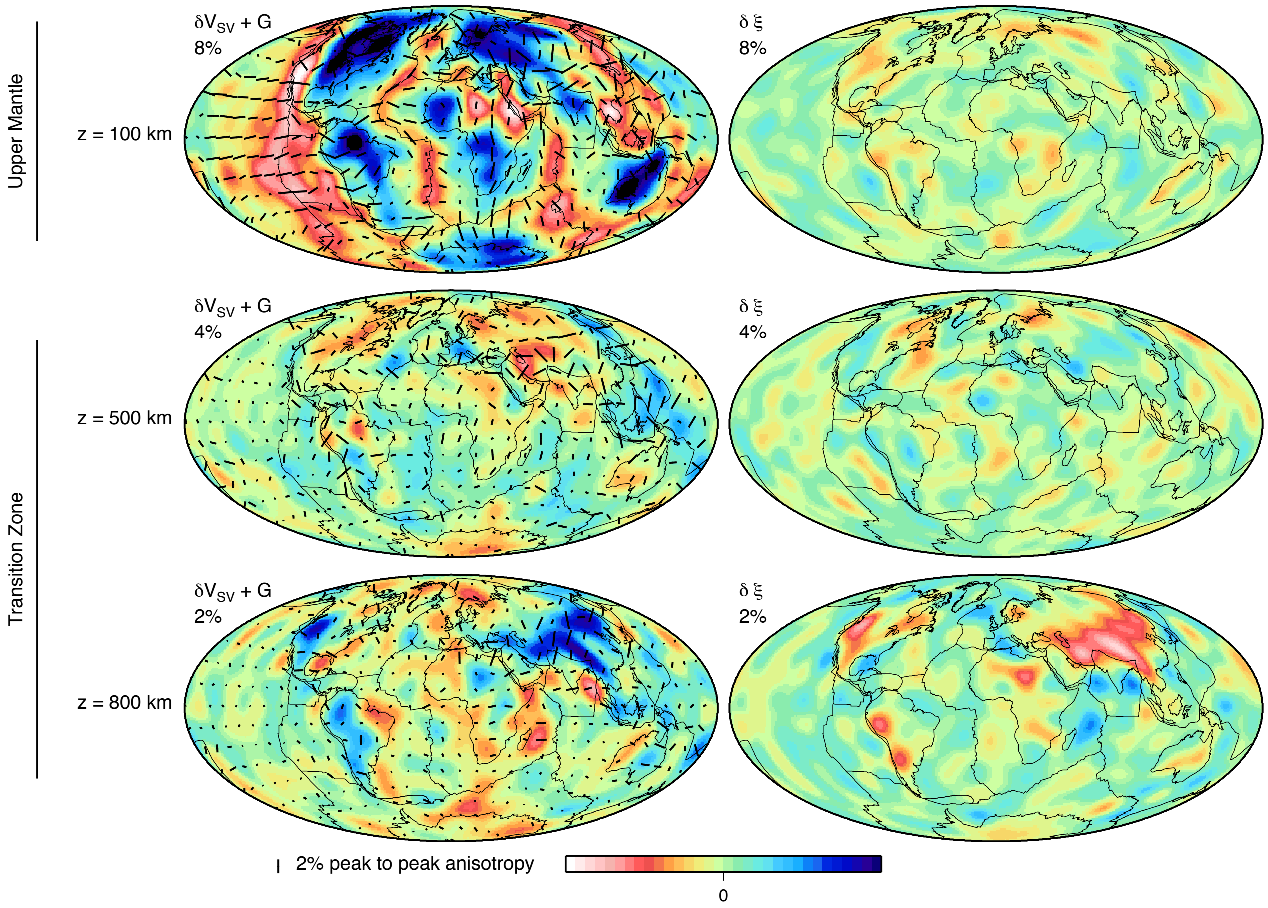

Figure 1. Tomographic images of the S-wave velocity V_{SV}, azimuthal anisotropy G (left) and radial anisotropy $\delta\xi = \xi - \xi_{ref}$ (right) in different mantle layers: The upper mantle, at 100 km in depth (top). The transition zone, at 500 km (middle) and 800 km (bottom) in depth. $\delta\xi$ is plotted with respect to an average reference model, $\xi_{ref} = 2.7\%$ at 100km, -1.5% at 500km, 0.4% at 800km. The error bars are calculated as in Burgos et al. (2014) and presented in Burgos (2013). Error bars on ξ and G are everywhere smaller than 1% and even smaller than 0.5% in well covered regions of the northern hemisphere. The color scale varies with depth and its range is defined at the top left of each figure.

spectra can be related to the spatial wavelength Λ through the relationship $\Lambda = \frac{2\pi a}{\ell+0.5}$, where a is the radius of the Earth. Rapid decreases in the amplitudes of the S-wave and the azimuthal parameter G are observed between 200 km and the different depths of the MTZ. Degree 2 of the spherical harmonics expansion is dominant in the UMTZ (Figure 2, 500 km, 600 km), but there is a change in the pattern of the S-wave velocity in the LMTZ at 700 km in depth, which is dominated by degree 1 and a decrease in the power spectrum, with the angular order ℓ related to the inverse of the spatial wavelength Λ. This is in agreement with the results of Kustowski et al. (2008), who observed a change in the heterogeneity distribution around the 660-km discontinuity. The spectral amplitude of parameter G is always smaller than the spectral amplitude of the $S-$wave velocity heterogeneity,

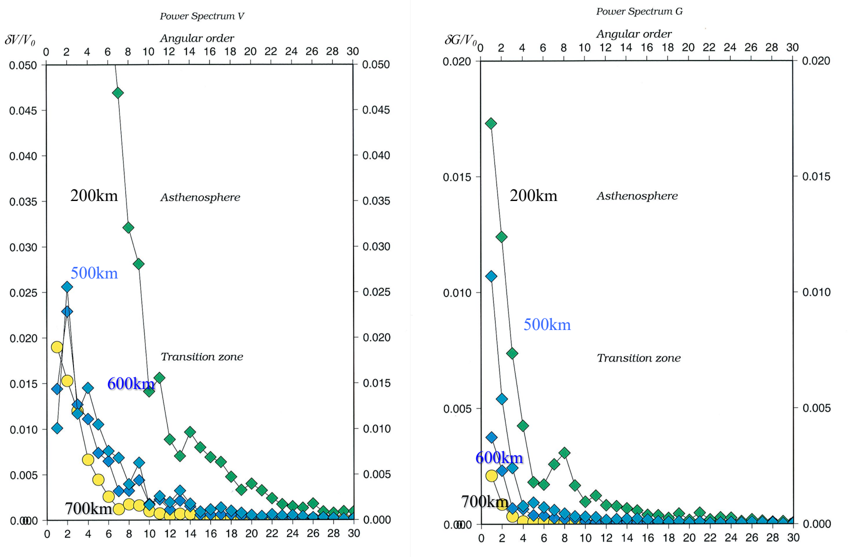

Vsv

G

Figure 2. Power spectra of the relative variations of S_V-wave velocity (Left) and of the azimuthal anisotropy G (Right) at different depths: Asthenosphere, 200 km; Transition zone: 500 km, 600 km and 700 km, as indicated. 200km: green diamonds; 500km: light blue diamonds; 600km: dark blue diamonds; 700km: yellow circles.

which can be understood considering the predominant contribution of the oceanic regions away from subduction zones ($\sim 2/3$ of the Earth surface) with a small value of parameter G in MTZ. The areas where the amplitude of parameter G is significant (subducting zones and central Asia) finally have a limited influence on the global average. The distributions of azimuthal and radial anisotropies found by different tomographic models (Yuan & Beghein 2013; Schaeffer et al. 2016; Debayle et al. 2016) are in poor agreement which is due to the small amplitude of anisotropy in MTZ often within their error bars. Another approach for studying MTZ azimuthal anisotropy was proposed by Huang et al. (2019) by using long-period SS precursors. It confirms the weakness of anisotropy in most oceanic areas except around subduction zones. Consequently, we now focus on the only areas where azimuthal anisotropy is significant, above the error bars, i.e. subduction zones and Central Asia.

3 THE UNIQUE ANISOTROPY BENEATH CENTRAL ASIA

The azimuthal anisotropy in the MTZ as displayed in Figure 1 is well correlated with subducting plate slabs and is relatively small in other regions, with the noticeable exception of central Asia. Fast V_{SV} and negative ξ radial anisotropy is also observed in Canadian and Andean cordillera, but their lateral extension is much smaller than in Central Asia. The significant azimuthal anisotropy is limited to eastern Asia at 500 km in depth, but it extends through the whole of central Asia at 800 km in depth (Figure 3). Unfortunately, this region is not well covered by SS precursors as investigated by Huang et al. (2019), making a comparison impossible. The puzzling azimuthal anisotropy in this

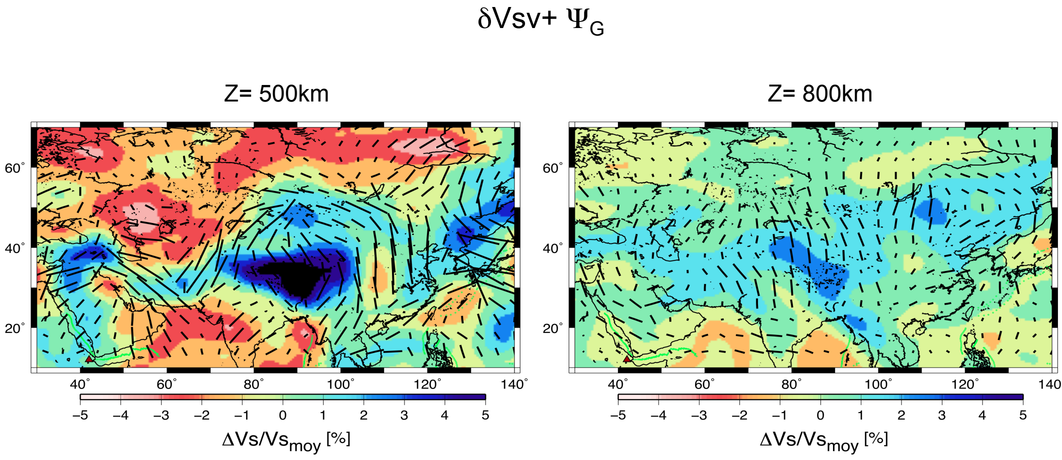

Figure 3. Tomographic images of S-wave velocity V_{SV}, azimuthal anisotropy G, in the central Asia transition zone at depths of 500 km (left) and 800 km (right).

region can be interpreted in terms of the mineralogy and/or the large-scale remnant plate structures and mantle convective flow. The mineralogical interpretation of the seismic anisotropy in the upper and lower MTZ is still subject of large uncertainties (e.g. the review of Mainprice (2015). In the UMTZ (410-660 km in depth), the 410-km discontinuity, attributed to the transformation from olivine to wadsleyite (orthorhombic), might result in a decrease in the anisotropy. A weaker discontinuity at 520 km in depth, e.g., Shearer (1996), has been attributed to the transformation from wadsleyite to ringwoodite. Wadsleyite (anhydrous or hydrous) can be strongly anisotropic whereas ringwoodite has a low anisotropy. This anisotropy might also be due to petrological layering caused by garnet-rich and ringwoodite-rich layers of transformed subducted oceanic crustal material (Karato 1998). However, notwithstanding some subduction zones where a tilted layering might be present, the resulting VTI medium would not cause any splitting for vertically propagating S-waves, nor produce the azimuthal anisotropy that is observed by Trampert & van Heijst (2002); Yuan & Beghein (2013); Debayle et al. (2016); Schaeffer et al. (2016) and in the present study. From 660-km to 900-1000-km deep (the LMTZ), the observed anisotropy might be due to the Bridgmanite lattice preferred orientation (and possibly to ferropericlase) that is caused by the deformation in the convective boundary layer at the top of the lower mantle (Karato 1998). Its lower limit might be related to a weak seismic discontinuity at 920 km, as identified by Kawakatsu & Niu (1994) in several subduction zones. The mineralogy of the MTZ (not only subducted plates but as well other regions) is relatively complex, and different minerals were identified (Vacher et al. 1998; Anderson 2007) which can give rise to seismic anisotropy. The mineral stishovite SiO2 that is probably present in subducting oceanic plates is strongly anisotropic, and it might contribute to the observed anisotropy. Akimotoite, which is the ilmenite form of MgSiO3, might dominate in cold parts of the transition zone, i.e. in areas near subduction zones (Shiraishi et al. 2008; Cottaar & Deuss 2016). Akimotoite has higher velocities than garnet at similar depths in hotter regions of the transition zone, and can produce a local high velocity that can be misinterpreted as a pile-up of subducted materials. So significant azimuthal anisotropy might be observed where the akimotoite content is high. A typical structure of perovskite may be cubic, but, in the LMTZ, when the crystal lattice is subject to strong distortion, silicate perovskites are in the orthorhombic crystal system. Bridgmanite is anisotropic (Meade et al. 1995; Mainprice et al. 2008) and a good candidate for explaining anisotropy in LMTZ since the CPO pattern and dominant slip system were carefully investigated (Tsujino et al. 2016) but still controversial (Kraych et al. 2016). Ferropericlase is nearly isotropic in the LMTZ but its anisotropy strongly increases with pressure and might be as large as 40% in the lower mantle.

A role for water can also be considered here. It was suggested that the MTZ might be a water reservoir (van der Meijde et al. 2003; Bercovici & Karato 2003) that collects the water from the subducting plates through hydrous minerals. The effect of water on CPO and slip systems was extensively investigated since hydrous wadsleyite might store a large amount of water transported by subducting slabs. But there is still some debates on the dominant slip systems able to generate seismic anisotropy (Tommasi et al. 2004; Kawazoe et al. 2013). A significant water content near subducted slabs (Chang & Ferreira 2019) can change the rheology of minerals (i.e., their viscosity and melting (Ohuchi et al. 2014; Ritterbex et al. 2015, 2020)). However, Ohuchi et al. (2014) argued that, due to changes in slip systems, anisotropy becomes weak if the UMTZ is hydrous and strong anisotropy near subducted slabs means a dry UMTZ (Ferreira et al. 2019). So, water transportation alone cannot explain this strong anisotropy and other mechanisms must be found (Ritterbex et al. 2015, 2020).

Nevertheless, we observe significant anisotropy in and around subducting plates, because they are specific places where the physical conditions of strong deformation are fulfilled for the development of the preferred orientation of minerals or of fine layering. In addition, central Asia is the continent below which many oceanic plates subduct or have subducted. In particular, the Tethys plate and the Izanagi plate (now extinct in the Pacific Ocean; see Lithgow-Bertelloni & Richards (1998); Scotese & Golonka (1997)) subducted beneath Eurasia for more than 100 Ma (see Torsvik et al. (2010) for kinematic plate reconstruction). As the Tethys and Izanagi and nowadays Pacific plates subduct in orthogonal directions under the Asian continent, some strong interaction and even collision might occur between these plates beneath central Asia. The Tethys plate moved northward before descending into the lower mantle (van der Hilst et al. 1997), whereas the Izanagi plate became stagnant in the MTZ (Fukao et al. 1992).

In order to investigate the convective flow below Asia, we also made some comparisons with geo-

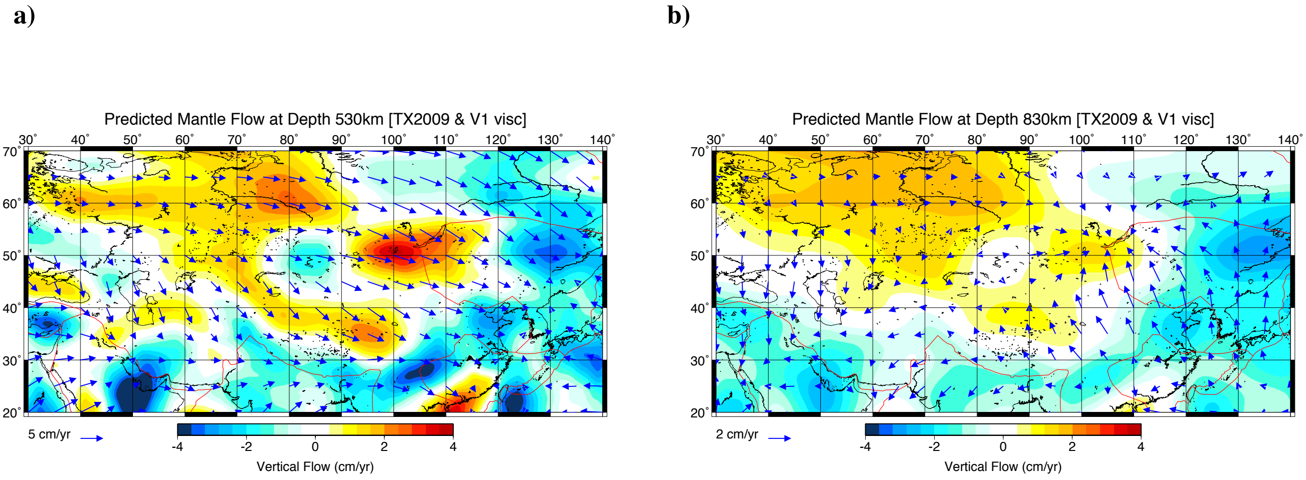

Figure 4. Flow models computed according to Simmons et al. (2009), for the depths of 500-550 km (a) and 800-850 km (b) (Courtesy of Alessandro Forte).

dynamic models. In the mantle circulation models of Simmons et al. (2009), it is observed (Figure 4a, b) that the flow patterns drastically change between 500 km and 800 km in depth. A more quantitative comparison of slab volume and past kinematics as done by Hafkenscheid et al. (2006) is a future path of research but is beyond the scope of this paper. The approach of Simmons et al. (2009) is based on the joint interpretation of seismic and geodynamic data (Nuvel-1 plate velocity model (DeMets et al. 2010), free air gravity data, dynamic topography) requiring mineral physical parameters linking seismic velocity to density perturbations in the Earth's mantle. The viscosity profile derived from convection models and GIA (global isostatic adjustment) data presents a minimum in the depth range 520-650km depth and a maximum around 1500- 2000km depth. Some hypotheses used in Simmons et al. (2009) are questionable, but these simulations produce flow patterns consistent with the different patterns in azimuthal anisotropy between 500km depth and 800km depth predicted by our tomographic inversions. Beneath central Asia, the flow at 530 km in depth is primarily horizontal West-to-southeast, whereas it is primarily oriented East-to-northwest at 830 km in depth. This might correspond to the remnant of the Izanagi plate which subducted beneath east Asia until 100 Ma ago (i.e., Torsvik et al. (2010)). The directions of the anisotropy (Figure 3) and flow (Figure 4) are poorly correlated at both of these depths, with large angle differences between them. The important observation here is that the large change in anisotropy direction between the UMTZ and LMTZ is also associated with the dramatic change in the flow orientation. Further geodynamic modeling is necessary, as this depends on the chosen tomographic model and the viscosity profile. Some alternative modeling has been tried (e.g., Becker et al. (2008)), but as long as the orientation mechanisms of the minerals in the MTZ are not so well understood, there is little rationale to go further in the interpretation. In the absence of consensus for the dominant mechanisms of alignment of bridgmanite-ferropericlase, it is difficult to reach strong conclusions, and a better understanding of the mineralogical processes in play in the seismic anisotropy of the MTZ will be necessary to reconcile the flow pattern directions and the observed anisotropy directions.

So far, past ridge processes were investigated by seismic anisotropy in ophiolites (Nicolas et al. 1980; Nicolas & Christensen 1987; Peselnick & Nicolas 1978). The recent investigation of seismic anisotropy beneath and around subduction zones (Nowacki et al. 2015; Ferreira et al. 2019; Sturgeon et al. 2019) provide new insights into our understanding of convective processes and the coupling between the upper and the lower mantles. What is observed at the global scale, e.g. the interaction between the remnant slabs beneath the continent for central Asia is almost unique in the world, and leaves an imprint through seismic anisotropy. The cluttering of the plate slabs in the MTZ might explain why some of the plates descend, why some others do not, and why some are stagnant in the lower transition zone. In addition to anisotropic minerals, several conditions must be fulfilled to observe the seismic anisotropy in the MTZ, the large-scale deformation field, and/or the probability of the presence of water carried by the subducting plates. These conditions are only present in subduction zones and beneath central Asia, where past subducting plates might have accumulated not only in the upper transition zone (UMTZ: 410-660 km in depth), but also in the lower transition zone (LMTZ: 660-1000 km in depth). The presence of subducting material present at the same time in multiple depth ranges of MTZ would explain why anisotropy might be significant only in specific regions of the transition zone.

REFERENCES

Anderson, D., 1961. Elastic wave propagation in layered anisotropic media, *J. Geophys. Res.*, **66**, 2953–2963.

Anderson, D., 2007. *New theory of the Earth*, Cambridge University Press, 2nd edn.

Auer, L., Boschi, L., Becker, T., Nissen-Meyer, T., & Giardini, D., 2014. Savani: A variable resolution whole-mantle model of anisotropic shear velocity variations based on multiple data sets, *Journal of Geophysical Research: Solid Earth*, **119**(4), 3006–3034.

Backus, G., 1962. Long-wave anisotropy produced by horizontal layering, *J. Geophys. Res.*, **67**, 4427–4440.

Becker, T., Ekström, J. K. G., & O'Connell, R., 2003. Comparison of azimuthal seismic anisotropy from surface waves and finite-strain from global mantle-circulation models, *Geophys. J. Int.*, **155**, 696–714.

Becker, T., Kustowski, B., & Ekström, G., 2008. Radial seismic anisotropy as a constraint for upper mantle rheology, *Earth and Planetary Science Letters*, **267**(1), 213–227.

Beghein, C., Resovsky, J., & van der Hilst, R., 2008. The signal of mantle anisotropy in the coupling of normal modes, *Geophys. J. Int.*, **175**, 1209–1234.

Bercovici, D. & Karato, S.-I., 2003. Whole-mantle convection and the transition-zone water filter, *Nature*, **425**, 39–44.

Beucler, E. & Montagner, J.-P., 2006. Computation of large anisotropic seismic heterogeneities., *Geophys. J. Int.*, **165**, 447–468.

Beucler, E., Stutzmann, E., & Montagner, J.-P., 2003. Measuring surface wave higher mode phase velocities using a rollercoaster type algorithm., *Geophys. J. Int.*, **155**, 289–307.

Burgos, G., 2013. *Tomographie du Manteau Supérieur par Inversion des Ondes de Surface*, Ph.D. thesis, Institut de Physique du Globe de Paris (IPGP).

Burgos, G., Montagner, J.-P., Beucler, E., Capdeville, Y., Mocquet, A., & Drilleau, M., 2014. Oceanic lithosphere-asthenosphere boundary from surface wave dispersion data, *Journal of Geophysical Research: Solid Earth*, **119**(2), 1079–1093.

Chang, S.-J. & Ferreira, A. M., 2017. Improving global radial anisotropy tomography: the importance of simultaneously inverting for crustal and mantle structure, *Bulletin of the Seismological Society of America*, **107**(2), 624–638.

Chang, S.-J. & Ferreira, A. M., 2019. Inference on water content in the mantle transition zone near subducted slabs from anisotropy tomography, *Geochemistry, Geophysics, Geosystems*.

Chang, S.-J., Ferreira, A. M., Ritsema, J., Heijst, H. J., & Woodhouse, J. H., 2015. Joint inversion for global isotropic and radially anisotropic mantle structure including crustal thickness perturbations, *Journal of Geophysical Research: Solid Earth*, **120**(6), 4278–4300.

Chen, M. & Tromp, J., 2007. Theoretical and numerical investigation of global and regional seismic wave propagation in weakly anisotropic earth models, *Geophys. J. Int.*, **168**, 1130–1152.

Christensen, N. & Lundquist, S., 1982. Pyroxene orientation within the upper mantle, *Bull. Geol. Soc. Am.*, **93**, 279–288.

Cottaar, S. & Deuss, A., 2016. Large-scale mantle discontinuity topography beneath europe: Signature of akimotoite in subducting slabs, *Journal of Geophysical Research: Solid Earth*, **121**(1), 279–292.

Debayle, E., Dubuffet, F., & Durand, S., 2016. An automatically updated s-wave model of the upper mantle and the depth extent of azimuthal anisotropy, *Geophysical Research Letters*, **43**(2), 674–682.

DeMets, C., Gordon, R. G., & Argus, D. F., 2010. Geologically current plate motions, *Geophysical Journal International*, **181**(1), 1–80.

Durand, S., Debayle, E., Ricard, Y., Zaroli, C., & Lambotte, S., 2017. Confirmation of a change in the global shear velocity pattern at around 1000 km depth, *Geophysical Journal International*, **211**(3), 1628–1639.

Dziewonski, A. & Anderson, D., 1981. Preliminary reference earth model., *Phys. Earth Planet. Int.*, **25**, 297–356.

Ferreira, A., Woodhouse, J., Visser, K., & Trampert, J., 2010. On the robustness of global radially anisotropic surface wave tomography, *Journal of Geophysical Research: Solid Earth*, **115**(B4).

Ferreira, A. M., Faccenda, M., Sturgeon, W., Chang, S.-J., & Schardong, L., 2019. Ubiquitous lower-mantle anisotropy beneath subduction zones, *Nature Geoscience*, **12**(4), 301–306.

Forsyth, D., 1975. The early structural evolution and anisotropy of the oceanic upper mantle, *GJras*, **43**, 103–162.

French, S. & Romanowicz, B., 2014. Whole-mantle radially anisotropic shear velocity structure from spectral-element waveform tomography, *Geophysical Journal International*, **199**(3), 1303–1327.

Fukao, Y., Obayashi, M., Inoue, H., & Nenbai, M., 1992. Subducting slabs stagnant in the mantle transition zone, *J. Geophys. Res.*, **97**, 4,809–4,822.

Fukao, Y., Nishida, K., Suda, N., Nawa, K., & Kobayashi, N., 2002. A theory of earth's background free oscillations, *Journal of Geophysical Research*, **107, B9**, 2206.

Gaboret, C., Forte, A., & Montagner, J.-P., 2003. The unique dynamics of the pacific hemisphere mantle and its signature on seismic anisotropy, *Earth PLanet. Sci. Lett.*, **208**, 219–233.

Hafkenscheid, E., Wortel, M., & Spakman, W., 2006. Subduction history of the tethyan region derived from seismic tomography and tectonic reconstructions, *Journal of geophysical research: Solid Earth*, **111**(B8).

Hess, H., 1964. Seismic anisotropy in exploration seismics, *Nature*, **203**, 629–631.

Huang, Q., Schmerr, N., Waszek, L., & Beghein, C., 2019. Constraints on seismic anisotropy in the mantle transition zone from long-period ss precursors, *Journal of Geophysical Research: Solid Earth*, **124**(7), 6779–6800.

Karato, S.-I., 1998. Seismic anisotropy in the deep mantle, boundary layers and the geometry of mantle convection, *Pure appl. Geophys.*, **151**, 565–587.

Kawakatsu, H. & Niu, F., 1994. Seismic evidence for a 920km discontinuity in the mantle, *Nature*, **371**, 301–305.

Kawakatsu, H., Kumar, P., Takei, Y., T., M. S., Kanazawa, Araki, E., & Suyehiro, K., 2009. Seismic evidence for sharp lithosphere-asthenosphere boundaries of oceanic plates, *Science*, **324**, 499–502.

Kawazoe, T., Ohuchi, T., Nishihara, Y., Nishiyama, N., Fujino, K., & Irifune, T., 2013. Seismic anisotropy in the mantle transition zone induced by shear deformation of wadsleyite, *Physics of the Earth and Planetary Interiors*, **216**, 91–98.

Kraych, A., Carrez, P., & Cordier, P., 2016. On dislocation glide in mgsio3 bridgmanite at high-pressure and high-temperature, *Earth and Planetary Science Letters*, **452**, 60–68.

Kustowski, B., Ekström, G., & Dziewonski, A., 2008. Anisotropic shear wave velocity of the earth's mantle: a global model. j. geophys. res. 113. doi:10.1029/ 2007jb005169, *J. Geophys. Res.*, **113**.

Lithgow-Bertelloni, C. & Richards, M. A., 1998. The dynamics of cenozoic and mesozoic plate motions, *Reviews of Geophysics*, **36**(1), 27–78.

Long, M. & Becker, T., 2010. Mantle dynamics and seismic anisotropy, *Earth Planet. Sci. Lett.*, **297**, 341–354.

Love, A., 1944. *A treatise on the mathematical theory of elasticity*, Dover publ., New York.

Mainprice, D., 2015. Seismic anisotropy of the deep earth from a mineral and rock physics perspective, *Treatise on Geophysics*, **2**, 487–538.

Mainprice, D., Tommasi, A., Ferre, D., Carrez, P., & Cordier, P., 2008. Predicted glide systems and crystal preferred orientations of polycrystalline silicate Mg-Perovskite at high pressure: Implications for the seismic anisotropy in the lower mantle, *EARTH AND PLANETARY SCIENCE LETTERS*, **271**(1-4), 135–144.

Marone, F. & Romanowicz, B., 2007. Non-linear crustal corrections in high-resolution regional waveform seismic tomography, *Geophysical Journal International*, **170**(1), 460–467.

Meade, C., Silver, P., & Kaneshima, S., 1995. Laboratory and seismological observations of lower mantle anisotropy, *Geophys. Res. Letters*, **22**, 1293–1296.

Montagner, J., 2002. Low anisotropy channels below the pacific plate., *Earth Planet. Sci. Lett.*, **202**, 263–274.

Montagner, J.-P., 1986. Regional three-dimensional structures using long-period surface waves., *Ann. Geophys.*, **4**, 283–294.

Montagner, J.-P. & Jobert, N., 1988. Vectorial tomography -II. Application to the Indian ocean, *Geophys. J. Int.*, **94**, 309–344.

Montagner, J.-P. & Kennett, B., 1996. How to reconcile body-wave and normal-mode reference earth models?, *Geophys. J. Int.*, **125**, 229–248.

Montagner, J.-P. & Nataf, H.-C., 1986. A simple method for inverting the azimuthal anisotropy of surface waves., *J. Geophys. Res.*, **91**, 511–520.

Montagner, J.-P. & Tanimoto, T., 1991. Global upper mantle tomography of seismic velocities and anisotropies., *J. Geophys. Res.*, **96**, 20,337–20,351.

Moulik, P. & Ekström, G., 2014. An anisotropic shear velocity model of the earth's mantle using normal modes, body waves, surface waves and long-period waveforms, *Geophysical Journal International*, **199**(3), 1713–1738.

Nicolas, A. & Christensen, N., 1987. Composition, structure and dynamics of the lithosphere/asthenosphere system (eds. froidevaux, c. & fuchs, k.), *Am. Geophys. Union, Washington D.C.*, pp. 111–123.

Nicolas, A., Boudier, F., & Boullier, A., 1973. Mechanisms of flow in naturally and experimentally deformed peridotites, *Am. J. Sci*, **273**(10), 853–876.

Nicolas, A., Boudier, F., & Bouchez, J., 1980. Interpretation of peridotite structures from ophiolitic and oceanic environments, *Am. J. Sci*, **280**(Pt 1), 192–210.

Nowacki, A., Kendall, J.-M., Wookey, J., & Pemberton, A., 2015. Mid-mantle anisotropy in subduction zones and deep water transport, *Geochemistry, Geophysics, Geosystems*, **16**(3), 764–784.

Ohuchi, T., Fujino, K., Kawazoe, T., & Irifune, T., 2014. Crystallographic preferred orientation of wadsleyite and ringwoodite: Effects of phase transformation and water on seismic anisotropy in the mantle transition zone, *Earth and Planetary Science Letters*, **397**, 133–144.

Panning, M. P., Lekic, V., & Romanowicz, B. A., 2010. Importance of crustal corrections in the development of a new global model of radial anisotropy, *J. Geophys. Res.*, **115**.

Peselnick, L. & Nicolas, A., 1978. Seismic anisotropy in an ophiolite peridotite: Application to oceanic upper mantle, *Journal of Geophysical Research: Solid Earth (1978–2012)*, **83**(B3), 1227–1235.

Ritterbex, S., Carrez, P., Gouriet, K., & Cordier, P., 2015. Modeling dislocation glide in mg2sio4 ringwoodite: Towards rheology under transition zone conditions, *Physics of the Earth and Planetary Interiors*, **248**, 20–29.

Ritterbex, S., Carrez, P., & Cordier, P., 2020. Deformation across the mantle transition zone: A theoretical mineral physics view, *Earth and Planetary Science Letters*, **547**, 116438.

Schaeffer, A., Lebedev, S., & Becker, T., 2016. Azimuthal seismic anisotropy in the earth's upper mantle and the thickness of tectonic plates, *Geophysical Supplements to the Monthly Notices of the Royal Astronomical Society*, **207**(2), 901–933.

Scotese, C. R. & Golonka, J., 1997. *Paleogeographic atlas*, PALEOMAP Project, University of Texas at Arlington Arlington.

Shearer, P., 1996. Transition zone velocity gradients and the 520km discontinuity, *J. Geophys. Res.*, **101**, 3,053–3,066.

Shiraishi, R., Ohtani, E., Kanagawa, K., Shimojuku, A., & Zhao, D., 2008. Crystallographic preferred orientation of akimotoite and seismic anisotropy of tonga slab, *Nature*, **455**(7213), 657–660.

Silver, P. & Chan, W., 1991. Shear wave splitting and subcontinental mantle deformation, *J. Geophys. Res.*, **96**, 16,429 – 16,454.

Simmons, N., Forte, A., & Grand, S., 2009. Joint seismic, geodynamic and mineral physical constraints on three-dimensional mantle heterogeneity: Implications for the relative importance of thermal versus compositional heterogeneity, *Geophys. J. Int.*, **177**, 1284–1304.

Smith, M. & Dahlen, F., 1973. The azimuthal dependence of Love and Rayleigh wave propagation in a slightly anisotropic medium, *J. Geophys. Res.*, **78**, 3321–3333.

Sturgeon, W., Ferreira, A. M., Faccenda, M., Chang, S.-J., & Schardong, L., 2019. On the origin of radial anisotropy near subducted slabs in the midmantle, *Geochemistry, Geophysics, Geosystems*, **20**(11), 5105–5125.

Tanimoto, T. & Anderson, D., 1984. Mapping convection in the mantle, *Geophys. Res. Lett.*, **11**, 297–290.

Tarantola, A. & Valette, B., 1982. Generalized nonlinear inverse problems solved using least squares criterion, *Rev. Geophys. Space Phys.*, **20**, 219–232.

Tommasi, A., Mainprice, D., Cordier, P., Thoraval, C., & Couvy, H., 2004. Strain-induced seismic anisotropy of wadsleyite polycrystals and flow patterns in the mantle transition zone, *J. Geophys. Res.*, **102**, B12405.

Torsvik, T. H., Steinberger, B., Gurnis, M., & Gaina, C., 2010. Plate tectonics and net lithosphere rotation over the past 150my, *Earth and Planetary Science Letters*, **291**(1), 106–112.

Trampert, J. & van Heijst, H., 2002. Global azimuthal anisotropy inthe transition zone, *Science*, **296**, 1297–1299.

Tsujino, N., Nishihara, Y., Yamazaki, D., Seto, Y., Higo, Y., & Takahashi, E., 2016. Mantle dynamics inferred from the crystallographic preferred orientation of bridgmanite, *Nature*, **539**(7627), 81–84.

Vacher, P., Mocquet, A., & Sotin, C., 1998. Computation of seismic profiles from mineral physics: the importance of the non-olivine components for explaining the 660 km depth discontinuity, *Physics of the earth and planetary interiors*, **106**(3), 275–298.

van der Hilst, R., Widiyantoro, S., & Engdahl, E., 1997. Evidence for deep mantle circulation from global tomography, *Nature*, **386**, 578–584.

van der Meijde, M., Marone, F., Giardini, D., & van der Lee, S., 2003. Seismic evidence for water deep in earth's upper mantle, *Science*, **300**(5625), 1556–1558.

Vinnik, L. & Montagner, J.-P., 1996. Shear wave splitting in the mantle from ps phases, *Geophys. Res. Lett.*, **23**, 2449–2452.

Vinnik, L., Kosarev, G., & Makeyeva, L., 1984. Anisotropy in the lithosphere from observations of SKS and SKKS, *Proc. Acad. Sci. USSR Geol. Sci. Sect.*, **278**, 1335–1339.

Visser, K., Trampert, J., & Kennett, B., 2008. Global anisotropic phase velocity maps for higher mode love and rayleigh waves, *Geophys. J. Int.*, **172**, 1016–1032.

Wookey, J., Kendall, J.-M., & Barruol, G., 2002. Mid-mantle deformation inferred from seismic anisotropy, *Nature*, **415**, 777–780.

Yoshizawa, K. & Kennett, B., 2002. Nonlinear waveform inversion for surface waves with a neighbourhood algorithm: Application to multi-mode dispersion measurements., *Geophys. J.Int.*, **149**, 118–133.

Yuan, K. & Beghein, C., 2013. Seismic anisotropy changes across upper mantle phase transitions, *Earth and Planetary Science Letters*, **374**, 132–144.

Appendix

Tomographic method.

The 3D anisotropic tomographic method is a classical two-step inversion procedure. From a practical point of view, the same algorithm (Tarantola & Valette 1982) is used for both steps. The forward problem can be generally written as:

$$\mathbf{d} = \mathbf{g}(\mathbf{m}) \tag{1}$$

where $\mathbf{d}$ is the vector associated with the whole dataset, $\mathbf{m}$ is the model parameter space, and $\mathbf{g}$ is the functional relating $\mathbf{d}$ and $\mathbf{m}$. The sensitivity kernels K are derived by first-order perturbation theory from equation (1). To generate an improved parameter estimate m_k starting from an initial parameter model m_0, we use an iterative algorithm, as expressed in Tarantola & Valette (1982):

$$\mathbf{m_k} = \mathbf{m_0} + C_m K_{k-1}^T M^{-1}[\mathbf{d} - \mathbf{g}(\mathbf{m_{k-1}}) + K_{k-1}(\mathbf{m_{k-1}} - \mathbf{m_0})], \tag{2}$$

with

$$M = C_d + K_{k-1} C_m K_{k-1}^T$$

where K is the partial derivative matrix, $K_{k-1} = \frac{\partial g(m_{k-1})}{\partial m_{k-1}}$. C_d is the covariance function of the data $\mathbf{d}$, including the data uncertainties and possible correlations between the data, and C_m is the covariance function of the model parameters $\mathbf{m}$, limiting the accessible parameter space. The diagonal terms of the *a posteriori* covariance operator are also computed, in order to estimate the error bars on the final parameters.

In the first step, the higher mode phase velocities of the Rayleigh and Love waves are separately regionalized at different periods, to retrieve the different azimuthal terms of the local phase velocity. The azimuthal dependence due to the presence of a general slight anisotropic elastic medium is a homogeneous trigonometric polynomial up to degree 4ψ, where ψ denotes the azimuth of the horizontal wave vector, measured clockwise from the north. For a given point located at θ, ϕ and for a given angular frequency ω or period $T(= \frac{2\pi}{\omega})$, $V(\omega, \theta, \phi, \psi)$, the local phase velocity is defined as a perturbation of an isotropic or VTI (Vertical symmetry axis, Transversely Isotropic) reference velocity (denoted as $V_0(\omega, \theta, \phi)$), such that $V = V_0 + \delta V$. The velocity perturbation $\delta V(\omega, \theta, \phi, \psi)$ can be expanded as a Fourier series in ψ Smith & Dahlen (1973):

$$\delta V(\omega, \theta, \phi, \psi) = \frac{1}{2V_0}(A_0 + A_1 cos2\psi + A_2 sin2\psi + A_3 cos4\psi + A_4 sin4\psi]). \tag{3}$$

The five local functions $A_n(\omega, \theta, \phi)$ depend on ω, θ, ϕ. Figure A1 (and similarly Figure A2) presents some global maps of A_0 (the local phase velocity) and A_1, A_2 (the $2-\psi$ azimuthal anisotropy), A_3, A_4 (the $4-\psi$ azimuthal anisotropy) for the different Rayleigh wave (and Love wave) higher modes, at a

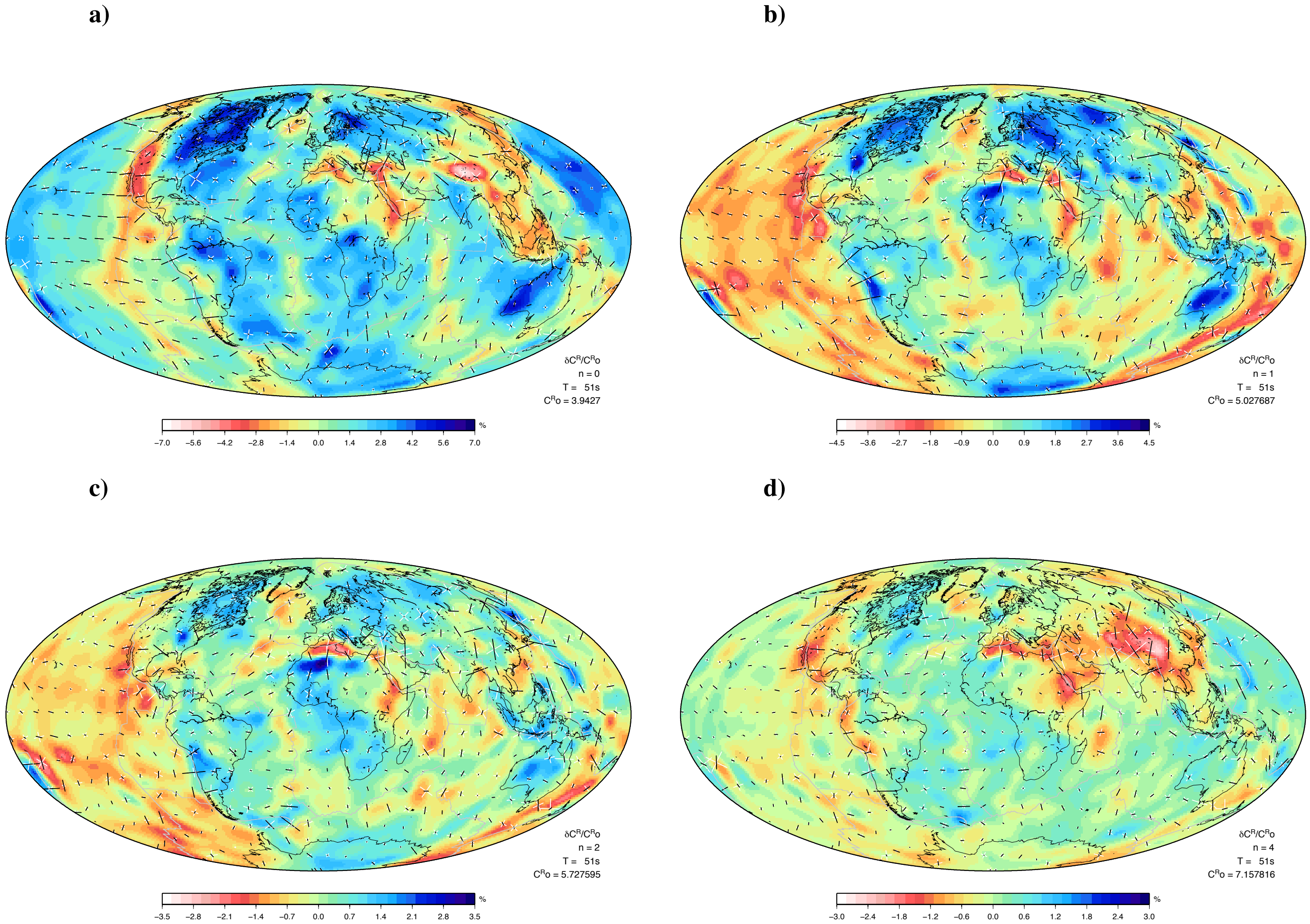

Figure A1. Phase velocity distributions of the different Rayleigh wave higher modes at the same period (T = 51 s). (a) n=0; (b) n=1; (c) n=2; (d) n=4. The black bars correspond to the maximum of $2-\Psi$ azimuthal terms (azimuthal anisotropy), and their lengths are proportional to their amplitudes.

period of 51 s. All $A_n(\omega, \theta, \phi)$ are related to some of the 21 anisotropic parameters p_j that describe the medium (Montagner & Nataf 1986; Chen & Tromp 2007). These are inverted at every point (θ, ϕ) in the second step of the tomographic technique for retrieving an estimate of the whole parameter space at a given depth.

$$\delta V(\omega, \theta, \phi, \Psi) = \frac{1}{V_0} \sum_{j=1}^{n_p=21} \int_0^{r_a} K_j(\omega, r, \theta, \phi, \Psi) \delta m_j(r, \theta, \phi) dr$$

However, all of the parameters cannot be reliably retrieved. Figure A3 shows examples of the higher mode sensitivity kernels of the Rayleigh (Figure A3a) and Love waves (Figure A3b) with respect to the SV-wave and SH-wave velocities. The sensitivity of the Rayleigh waves to V_{SH} is small, whereas the Love wave higher modes can be sensitive to V_{SV}. The maximum sensitivity at a given period

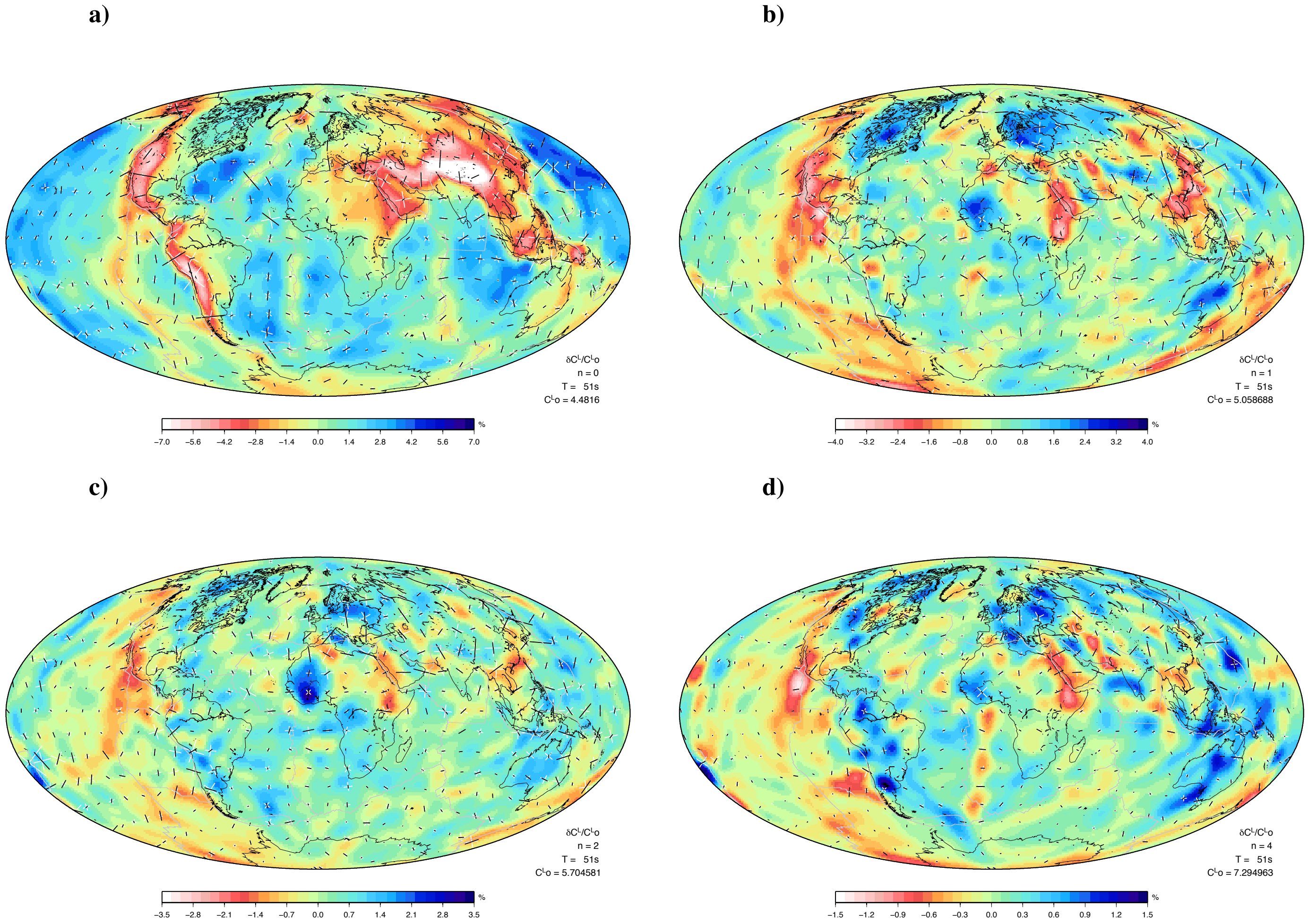

Figure A2. Phase velocity distributions of the different Love wave higher modes at the same period (T = 51 s). (a) n=0; (b) n=1; (c) n=2; (d) n=4.

increases with the order n of the higher mode. For example, the 4th Rayleigh higher mode (Figure A3a) at 51 s has a maximum sensitivity in V_{SV} at 800 km in depth. These kernels show that higher modes make it possible to obtain good depth resolution down to 1200 km, well below the upper (410-660 km) and lower (660-900 km) transition zones, even though we only show the results down to 800 km, which represents the main focus of the present study. Parameter G (and similarly parameter E) which expresses the $2-\psi$ (and $4-\psi$) azimuthal dependence of the SV-wave (and the SH-wave) has the same kernel as V_{SV} (and V_{SH}), and therefore it can also be recovered down to 1200 km in depth. V_{SV}, V_{SH}, G, Ψ_G, and E, Ψ_E are the most robust parameters that can be retrieved by the inversion at depth of the higher mode phase velocity distributions. Variations in ρ, V_{PV} and V_{PH} are scaled on these parameters, down to 410 km in depth Montagner & Tanimoto (1991), although they are free below this depth. The local crustal structure has also been inverted due to the shortest periods of the Rayleigh and Love wave dispersions in the datasets (Burgos 2013).

Resolution tests

We performed numerous synthetic tests to check the robustness of the inverted parameters $\xi, G, \Psi_G, E, \Psi_E$, by exploring different vertical correlation lengths, different weigthing between the fundamental modes and the overtones. Some of these examples are presented in Figure A4. We search for the depth resolution of the tomographic method by perturbing the depth profiles of V_{SV} and ξ at different depths using delta functions convolved with a Gaussian filter (Figure A4, green lines). We show examples at 300 km and 700 km in depth. The important result is that in both cases, the perturbations are retrieved at the correct depths. There is some spectral leakage towards other parameters V_{PH}, η, Φ, because we invert for five parameters, whereas we only have two independent pieces of information in this case. In addition, we can expect that in the real Earth, there should always be all kinds of anomalies for the five parameters that will occur simultaneously.

a) Rayleigh

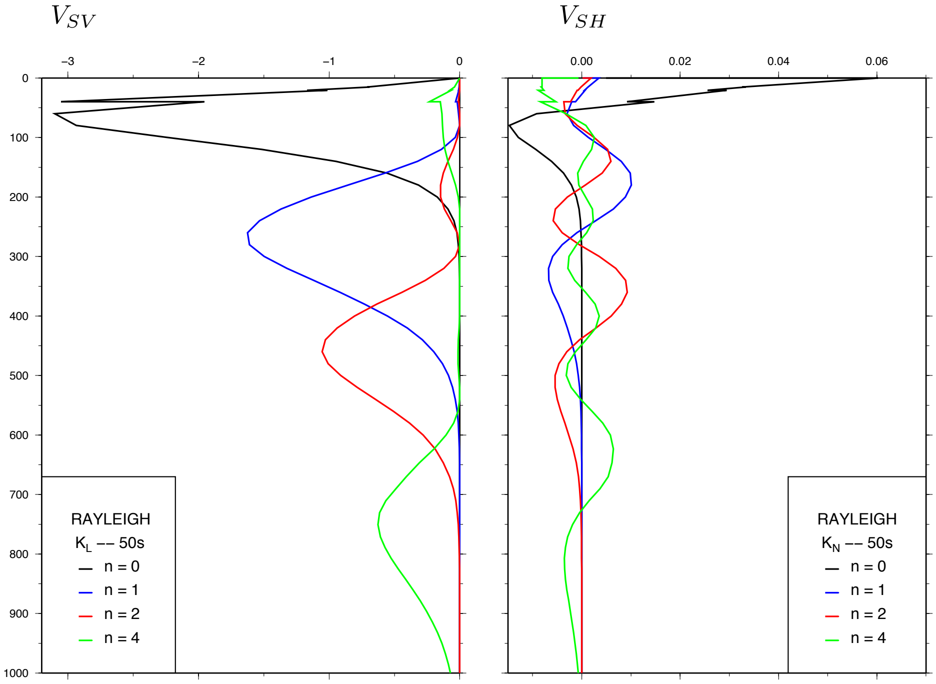

b) Love

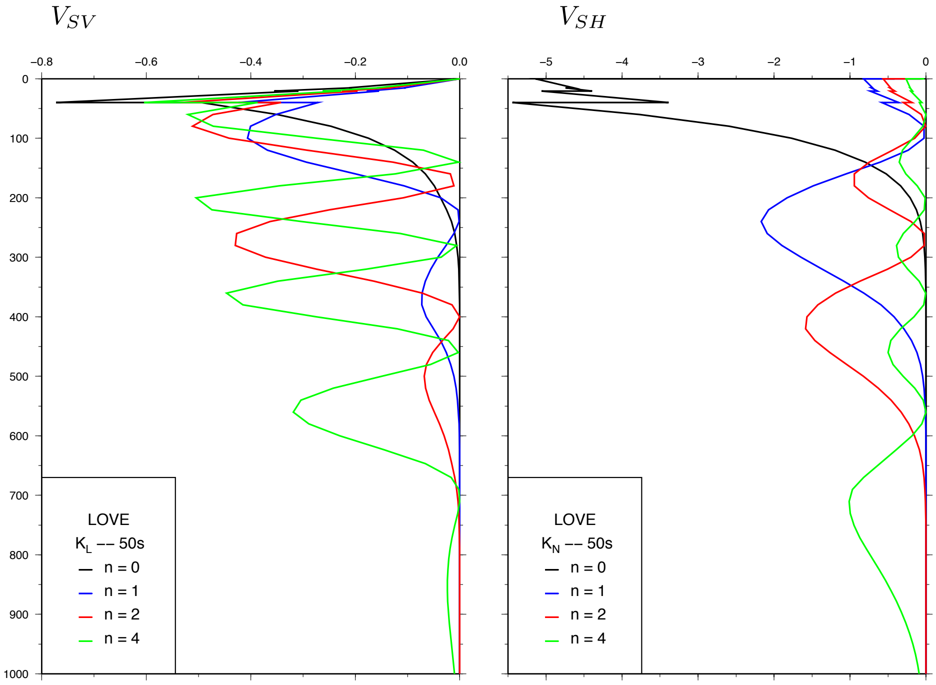

Figure A3. Phase velocity kernels of the different higher modes at the period T = 51 s. (a) Rayleigh waves. (b) Love waves. Left: L-kernel. Right: N-kernel. The elastic parameter L (and similarly N) is related to the V_{SV} velocity (and the V_{SH} velocity) by the relation $L = \rho V_{SV}^2$ (and $N = \rho V_{SH}^2$), where ρ is the density.

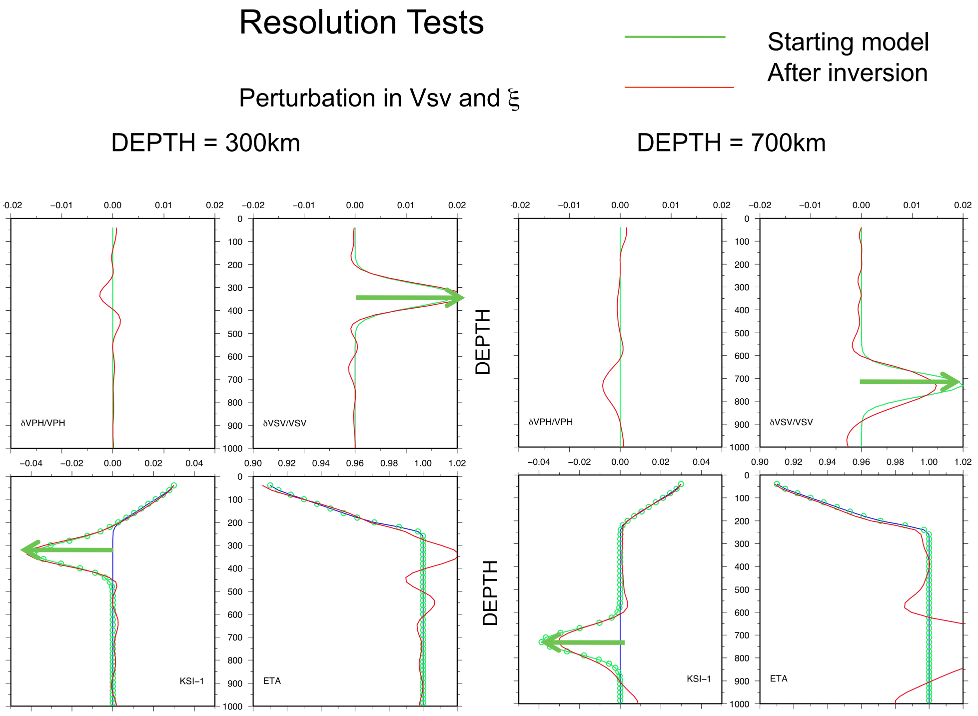

[h]

Figure A4. Resolution of the anisotropic parameters at the two different depths, of 300 km and 700 km.